Segregation, precipitation, and phase decomposition behavior of a carbon-doped non-equiatomic nanocrystalline CoCrFeMnNi high entropy alloy

Yemao Lu [a,b,c,d,*], Sangjun Kang [c,d], Gennadiy Salishchev [e], Anastasia Semenjuk [e], Xiang Chen [a], Christian Kübel [b,c,d], Horst Hahn [b], Yulia Ivanisenko [b]

[a] Nano and Heterogeneous Materials Center, Nanjing University of Science and Technology, Nanjing 210094, China
[b] Institute of Nanotechnology, Karlsruhe Institute of Technology, Kaiserstraße 12, Karlsruhe 76131, Germany
[c] Karlsruhe Nano-Micro Facility, Karlsruhe Institute of Technology, Hermann-von-Helmholtz-Platz 1, Eggenstein-Leopoldshafen 76344, Germany
[d] Institute of Material Sciences, Technical University Darmstadt, Peter-Grünberg-Straße 2, Darmstadt 64287, Germany
[e] Laboratory of Bulk Nanostructured Materials, Belgorod State University, Belgorod 308015, Russia

Keywords:
High entropy alloys
Segregation
Precipitation
Transmission electron microscopy
Atom probe tomography

A B S T R A C T

Elemental segregation at grain boundaries significantly influences the mechanical and functional properties of materials through structural and compositional changes. This phenomenon is especially common in high entropy alloys (HEAs) composed of multi-principal elements. Understanding the behavior and evolution of elemental segregation at grain boundaries is essential for tailoring material properties. In this study, we investigated the segregation, precipitation, and phase decomposition behavior of a nanocrystalline non-equiatomic CoCrFeMnNi HEA with intentional doping C interstitials, subjected to isochronal annealing treatments. Microstructure characterization using electron microscopies and atom probe tomography suggests that the nanocrystalline FCC solid solution decomposed during annealing at 500 °C, leading to the formation of CoFe B2 and NiMn FCC phases together with significant decoration of grain boundaries by Ni—Mn and C—Cr co-segregations. Furthermore, annealing at higher temperatures accelerated the precipitation of Cr carbides, CoFe B2 and NiMn FCC phases. However, the intermetallic particles were not observed after annealing at the evaluated temperatures, while the carbides persisted. It is proposed that diffusion processes were accelerated in the nanocrystalline HEA due to the high density of lattice defects. These findings provide detailed insight into the sequence and mechanisms of decomposition, from initial elemental segregation to precipitation in HEAs.

1. Introduction

High entropy alloys (HEAs) or compositionally complex alloys (CCAs) developed independently by Cantor and Yeh et al. have attracted increasing attention in the past two decades [1,2]. HEAs are historically defined as alloys consisting of five or more elements with a concentration of each element of 5–35 at.%. The equiatomic CoCrFeMnNi alloy, a single face-centered cubic (FCC) phase solid solution, was initially reported by Cantor. However, it was later discovered that this alloy undergoes phase decomposition upon annealing in the intermediate temperature range of 500–700 °C, forming a Cr-rich body-centered cubic (BCC) phase, a Cr-rich σ phase, an $L1_0$-NiMn phase, and a B2-CoFe intermetallic compound [3–6]. Otto et al. reported that $L1_0$-NiMn, B2-CoFe and Cr-rich BCC phases precipitate at grain boundaries after annealing a coarse-grained CoCrFeMnNi alloy (grain size ~100 μm) at 500 °C for 500 days [4]. In contrast, Schuh et al. reveal that B2-CoFe and Cr-rich BCC phases formed in a nanocrystalline CoCrFeMnNi alloy with a grain size of ~50 nm after annealing at 450 °C for only 5 min [7]. This contrast highlights the well-established fact that smaller grain sizes provide fast diffusion paths, significantly accelerating phase formation during annealing in the CoCrFeMnNi system.

Carbon, as an interstitial, is often doped into HEAs to enhance solid solution strengthening [8–11] and strain hardening capability [12–15]. In the CoCrFeMnNi system, recent studies have shown that a moderate amount of carbon dissolved in the matrix contributes to improved lattice friction and strengthening. However, excessive C addition leads to the

* Corresponding author at: Nano and Heterogeneous Materials Center, Nanjing University of Science and Technology, Nanjing 210094, China.
E-mail address: yemao.lu@njust.edu.cn (Y. Lu).

formation of carbides at grain boundaries and within the grain interior, ultimately leading to a decrease of plasticity [16,17]. Another notable effect of C doping in HEAs is its role in reducing the saturated grain size during severe plastic deformation (SPD) [18,19], such as using high-pressure torsion (HPT). For example, 2 at.% C addition significantly promotes the saturated grain size decrease from 50 nm to 20 nm after the same HPT deformation conditions in the Co1Cr0.25Fe1Mn1Ni1 HEA [20]. This leads to an increase of yield strength from 1.7 GPa to 2.4 GPa, reasonably associated with a dramatic reduction of ductility. It was also found that the addition of only 1200 ppm carbon increases the hardness of the HPT-processed high-purity Ni sample from 3.19 GPa to 5.15 GPa [21]. During SPD processing, numerous defects including grain boundaries are introduced. These defects not only enhance atomic diffusivity through grain boundary diffusion but also serve as abundant nucleation sites for elemental segregation and the precipitation of new phases. Carbon, as an interstitial element, tends to segregate at defect sites (e.g., dislocations and grain boundaries) after the SPD process [22,23], and the presence of such segregations can potentially influence the precipitation process during subsequent annealing.

Elemental segregation at grain boundaries significantly influences the mechanical and functional properties of materials through altering their structural and compositional states [7,24]. Recently, it was reported that Mo solute segregation at planar defects contributes to a significant increase in yield strength after post-deformation annealing of CrCoNi-based medium-entropy alloys with Mo alloying [25]. Similarly, elemental segregation at defects was found to increase both interfacial strength and ductility in the CoNiCrFe HEA system [26]. Therefore, understanding the underlying mechanisms of the phase decomposition and precipitation is essential for the design of new HEAs with tailored properties. Previous studies have primarily focused on phase formation during annealing and the corresponding thermodynamic aspects in the CoCrFeMnNi alloy at intermediate temperature range from 450 to 600 °C. However, the mechanism and progression from initial elemental segregation to phase decomposition and precipitation in nanocrystalline CoCrFeMnNi alloys remain unclear, particularly in the presence of interstitial carbon. In the present work, we systemically investigated the thermal stability of C-doped nanocrystalline CoCrFeMnNi alloy after isochronal annealing from 200 to 600 °C. Microstructural characterization was performed to reveal the sequence of microstructural evolution, from the onset of elemental segregation to precipitation of various phases and their eventual dissolution and grain growth.

2. Materials and methods

Non-equiatomic HEA $Co_1Cr_{0.25}Fe_1Mn_1Ni_1$ with nominally 2 at.% carbon and reduced Cr content, avoiding the formation of massive carbides was melted using high-purity elements (99.9 wt%) in a vacuum oven by induction [27]. The distribution of the principal elements in the as-cast alloy was determined by EDX in our previous study [20], which indicated a dendrite and interdendrite structure. Subsequently, disks for HPT processing were cut from the as-cast ingot with dimensions of ϕ 15× 0.8 mm^3. HPT was performed at room temperature under a hydrostatic pressure of 6.5 GPa for 3 turns to obtain a nanocrystalline structure. Differential scanning calorimetry (DSC) measurements were performed using a NETZSCH DSC 204F1 Phoenix calorimeter in a purified argon atmosphere with a heating rate of 20 °C/min. Annealing temperatures were selected according to the DSC measurement of the as-deformed alloy, shown in Fig. 1. The DSC profile of the as-deformed HEA reveals a broad exothermic reaction starting at 120 °C, which ends with a small peak at ~530 °C and a separate strong exothermic peak at ~600 °C, which could be related to precipitation and grain growth events [28], as confirmed by microstructure investigations below. Based on that, the HPT-processed samples were subjected to a post-deformation isochronal annealing in a high-vacuum quartz tube furnace for 1 h from 200 to 600 °C with an interval of 100 °C, and two extra increments (530 and 560 °C) between 500 °C and 600 °C, were added according to DSC results.

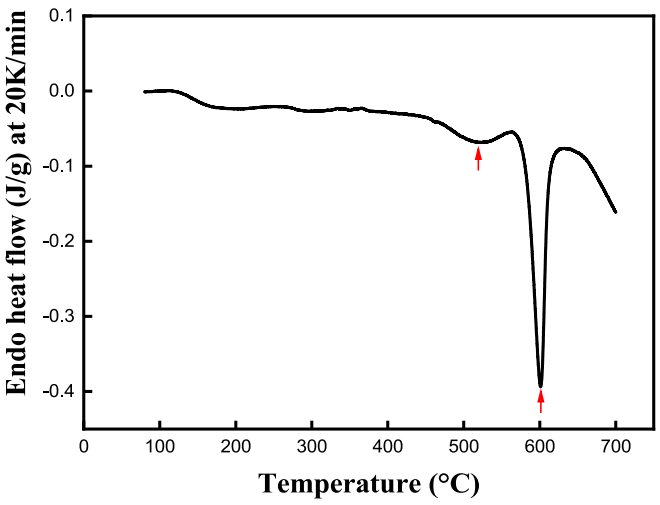

Fig. 1. DSC heating curve of the as-deformed alloy, a strong exothermic peak on 600 °C and one around ~530 °C.

Conventional bright-field transmission electron microscopy (BF-TEM), selected area electron diffraction (SAED), high-resolution TEM (HRTEM) and scanning transmission electron microscopy (STEM) were performed using Themis 300 and a Themis Z TEM from Thermo Fisher Scientific Inc., both operated at 300 kV and equipped with a Super-X energy dispersive X-ray spectrometer (EDX). STEM-based electron energy loss spectroscopy (EELS) spectra and maps were acquired on the Themis Z using a GIF continuum K3 Camera providing an energy resolution of 0.6 eV and a step size of 0.5–10 nm. The current for EELS acquisition ranges from 0.01 nA to 0.5 nA, depending on the data requirement. The collection and convergent semi-angle are 40 and 30 mrad, respectively. To define the collection and convergent angles, C2 aperture was set to 70 μm and the Gatan entrance aperture to 5 mm. Subsequent spectrum imaging (SI) analysis was performed using Digital Micrograph software, following core-loss edges: C K, Cr L, Mn L, Fe L, Co L, and Ni L. Atom probe tomography (APT) measurements were performed using CAMECA LEAP 4000 HR instrument in voltage mode with a pulse fraction of 30 %, a pulse rate of 200 kHz and a detection rate of 0.5 % at 55 K. The 3-dimensional reconstruction and further analysis were obtained using the AP Suite software. To ensure minimal overlap with grain and dendritic structures, TEM lamellae were prepared normal to the axial direction of the HPT disk, positioned 5 mm away from the disk center, representing the saturated microstructures. The APT tips and TEM lamellae were prepared using a FEI Strata 400 equipped with a Gallium focused ion beam (FIB) system.

3. Results

3.1. Chemical inhomogeneity of as-deformed alloy

As we have shown previously [20], the structure of the experimental alloy in the as-cast state is not chemically homogeneous and consists of dendrites. The dendrites exhibit higher Cr, Fe and Co content, whereas the interdendritic regions are rich in Ni and Mn. This is analogous to the structure of the as-cast CoCrFeMnNi alloy [1]. The compositional fluctuations in the as-cast alloy after HPT are shown in Fig. 2. Fig. 2 (a) shows the TEM lamellae prepared by FIB, with the investigated plane perpendicular to the tangential direction of the HPT disk. In Fig. 2 (b) one can see that severe plastic deformation had not led to a full chemical homogenization of the sample. The elemental distribution map indicates formation of a lamellar structure with alternating layers enriched in Cr, Co and Fe and enriched in Ni and Mn. Obviously, Cr, Co and Fe-rich lamellae are the remnants of dendrites and will be called in the

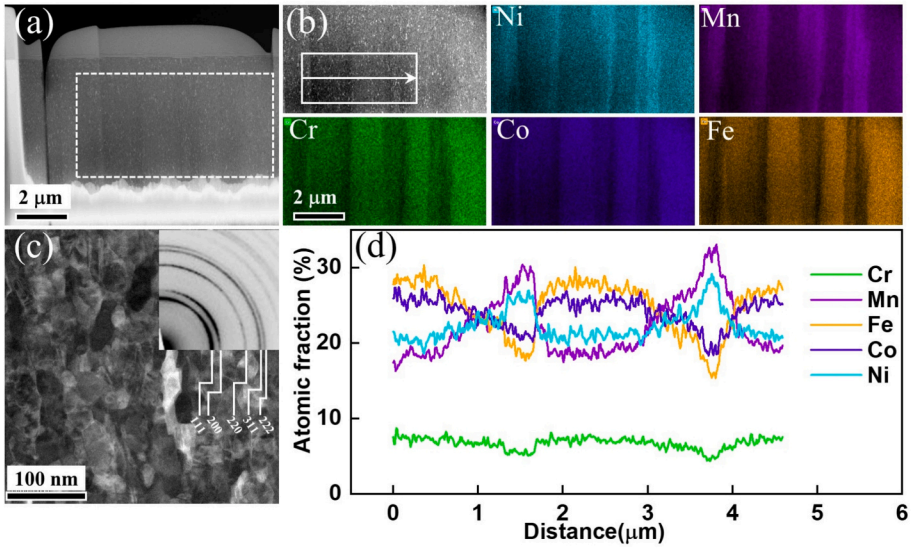

Fig. 2. Microstructure and elemental distribution of the as-deformed CoCrFeMnNi-C2 alloy: (a) HAADF-STEM overview image of the lamella prepared by FIB; (b) enlarged STEM image and corresponding EDX maps of the metallic elements; (c) HAADF-STEM image of the microstructure of the C2N3 alloy and inserted SAED pattern; (d) concentration profile created along the white arrow in (b).

following "dendritic bands" (DB), whereas Ni and Mn-rich lamellae resulted from severe deformation of interdendritic areas and will be called in the following "interdendritic bands" (IDB).

The high-angle annular dark-field (HAADF)-STEM image and the selected area electron diffraction pattern in Fig. 2 (c) reveal a single FCC phase, uniform nanocrystalline microstructure with slightly elongated grains. Independent of the compositional inhomogeneity discussed above, the grain size was refined to approximately 20 nm along the short axis in both the DB and the IDB regions. A concentration profile was measured along the white arrow as indicated in Fig. 2 (b) to determine the composition of each band as shown in Fig. 2 (d). The transition area between the DB and IDB regions appears primarily due to an inclination of the inter-region boundary in projection and the plastic deformation induced during HPT. In addition, noticeable concentration variations are observed between the two domains (Fig. 2 (d)). A statistical comparison based on SEM-EDX images and STEM-EDX maps indicates an area fraction of ~2/3 for DB and ~ 1/3 for IDB. The average concentrations of each element are presented in Table 1.

3.2. Microstructure after annealing

The brief microstructural evolution of the HPT-processed nanocrystalline HEA after isochronal annealing at different temperatures is depicted in Fig. 3 (a). Differentiating between the IDB and DB regions was not possible in the BF-TEM images, while this distinction can be clarified through subsequent spectroscopy investigations. At a low annealing temperature of 200 °C, the microstructure closely resembles that of the as-deformed state, exhibiting a nanocrystalline grain size of approximately 20 nm and a single FCC phase as determined by the corresponding diffraction pattern. A weak heat release in the DSC curve (Fig. 1), revealed in this temperature range, most likely corresponds therefore to recovery of severely deformed microstructure, including a relaxation of non-equilibrium grain boundaries. However, upon increasing the annealing temperature to 500 °C, faint additional reflections associated with a BCC structure emerge in the diffraction pattern. Except this, no conspicuous changes, including grain growth, are evident in this state, and the grain size remains comparable to that in the as-deformed state, at around 20 nm, indicating the stability of the HPT-deformed structure up to 500 °C. Following annealing at 530 and 560 °C, the BCC reflections become more pronounced in the diffraction patterns. At these elevated temperatures, the microstructure coarsens due to the growth of FCC grains and precipitates, which reflects in a first exothermic peak in DSC curve (Fig. 1). The mean grain size, averaged across all phases in the sample annealed at 530 and 560 °C, measures approximately 64 and 87 nm. At 600 °C, significant grain growth is observed accompanied by a second (strong) exothermic peak in DSC curve (Fig. 1), and the microstructure features equiaxed grains with an average size of about 280 nm. Alongside the grain growth, the BCC reflections are no longer visible, indicating the presence of a single FCC structure after annealing at this temperature. To better understand the structural evolutions of the HEA annealed at different temperatures, SAED profile analysis was performed for representative samples using a profile analysis of the SAED pattern (PASAD) [29] shown in Fig. 3 (b). The peak positions were determined by fitting a combined model to all peaks using pseudo-Voigt peak functions. Thus, the lattice parameters of the FCC phase and the BCC phase can be roughly estimated to be 3.61 Å and 2.88 Å, respectively.

Table 1
The average chemical composition with statistical error and area fraction of the DB and IDB regions in the as-deformed alloy.

Domains	area fraction	Chemical composition (at.%)				
		Cr	Co	Fe	Ni	Mn
DB	2/3	6.9 ± 0.6	25.9 ± 3.2	27.9 ± 3.5	20.0 ± 2.2	18.3 ± 2.1
IDB	1/3	4.8 ± 0.4	19.6 ± 2.6	17.1 ± 2.2	27.9 ± 3	30.6 ± 3.7

3.3. Segregation, FCC phase decomposition and secondary phase precipitation

3.3.1. Elemental segregation and new phase formation

To comprehend the FCC phase decomposition and new phases precipitating, a spectroscopic analysis using STEM-EELS SI was conducted for samples annealed in the temperature range between 500 and 600 °C for 1 h. In Fig. 4, the microstructure and elemental maps encompassing both the DB and IDB regions after heat treatment at 500 °C for 1 h are presented. Analogous to the bright-field TEM images in Fig. 3, the annular dark-field (ADF) STEM image in Fig. 4 depicts a nanocrystalline microstructure with a grain size of approximately 20 nm. STEM-EELS SI analysis reveals the formation of Fe/Co enriched

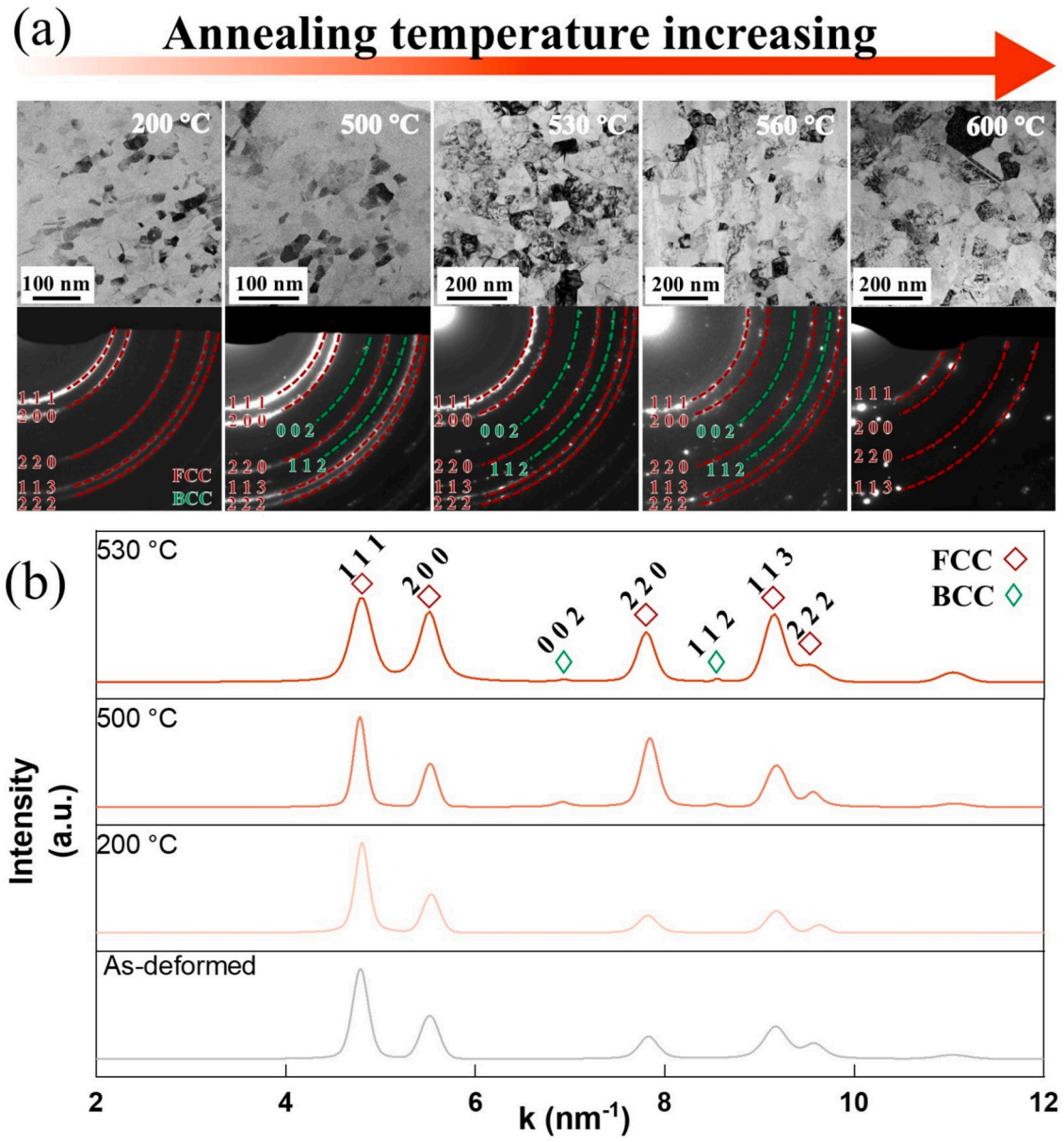

Fig. 3. (a) BF-TEM images and corresponding SAED of the samples after isochronal annealing from 200 to 600 °C for 1 h; (b) the profile of SAED patterns of the as-deformed sample and the samples annealed at 200 °C, 500 °C and 530 °C.

nanoparticles with a diameter of around 20 nm in the DB area (indicated with white arrows), while Ni/Mn-enriched nanoparticles with a diameter of approximately 5 nm are observed in the IDB area (indicated with red arrows). These two types of particles are largely assumed to correspond to the CoFe B2 and NiMn $L1_0$ phases, precipitated during the annealing of the Cantor alloy [30]. Furthermore, Cr elemental segregation is present in the analyzed area, observed at grain boundaries in both DB and IDB regions, corroborating the ADF-STEM image.

To investigate the complex segregation behavior at the grain boundaries, STEM-EELS SI analysis was conducted in the DB region with a step size of 0.5 nm, as shown in Fig. 5 (a). It revealed a heterogeneous distribution of Mn, Ni and Cr along grain boundaries. Notably, two distinct types of grain boundary decorations were observed in the EELS elemental maps. In certain regions of the grain boundary, Cr exhibits significant segregations, while Ni along with minor Mn preferentially segregate at other segments of the same grain boundary indicating heterogeneous segregation. Additionally, a high concentration of Ni and Mn appears near the CoFe particles, suggesting a potential nucleation site for the formation of the NiMn phase. The two types of segregation behavior along the grain boundary are clearly illustrated in Fig. 5 (a), as indicated for grains G1-G4.

Subsequently, nonnegative matrix factorization (NMF) analysis was applied to the acquired dataset, as shown in Fig. 5(b-c). Fig. 5(b) shows the spectra of the four distinct components extracted using the NMF method along with their spatial distribution in Fig. 5 (c), where the higher intensity in the component maps indicates greater contribution of each component. The detailed chemical composition of each component, calculated based on the spectra, is summarized in Table 2.

Component 1 represents high intensity at specific grain boundaries and granular features near the black hollow, which corresponds CoFe particle in Fig. 5 (a). Note that this particular elemental segregation only occurs at certain grain boundaries. Component 1 exhibits relatively higher Ni and Mn peaks compared to other components, suggesting the co-segregation of Mn and Ni at certain grain boundaries. Component 2 shows a relatively homogeneous distribution (Fig. 5 (c)). Its composition closely resembles that of the DB region but with a reduced Mn and Cr

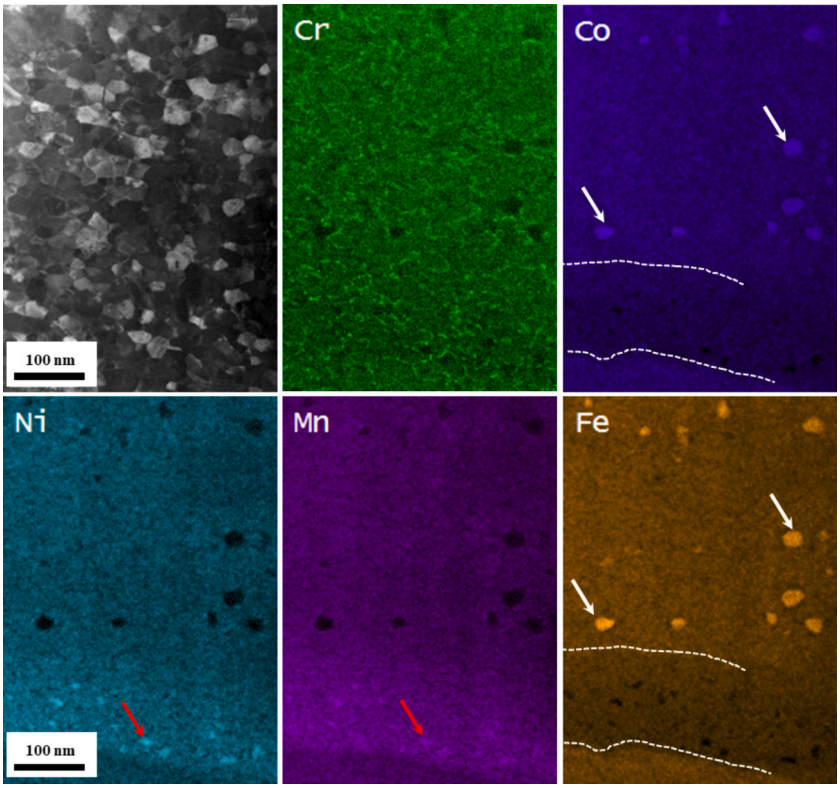

Fig. 4. STEM-EELS SI elemental maps for the metallic elements and corresponding ADF image of the sample annealed at 500 °C for 1 h.

content. Therefore, Component 2 can be identified as the matrix. Component 3 reveals another grain boundary segregation. Unlike Component 1, the regions where Component 3 exhibits high intensity corresponding to low-intensity regions in Component 1, and vice versa. The composition of Component 3 provided in Table 2 highlights an ultra-high Cr concentration (21.1 %) nearly three times its nominal content in the original sample. This suggests a distinct Cr segregation at certain grain boundaries. Component 4 appears as particles with high intensity in Fig. 5 (c). Based on its composition in Table 2, the particles are enriched with Co and Fe. Additionally, almost all grain boundaries show extremely low intensity suggesting that Co and Fe are largely depleted at grain boundaries.

The NMF analysis reveals the presence of two distinct types of grain boundary segregation, along with the emergence of new phases, demonstrating significant variations in their spatial distribution. One type of grain boundary segregation is dominated by Mn and Ni with minimal Cr signal. In contrast, other grain boundaries are characterized by a high Cr concentration with a notable depletion of Mn and Ni. Additionally, Cr and Ni—Mn segregated regions appear adjacent to newly formed CoFe particles, potentially acting as precursors for carbide and NiMn phase formation. These findings highlight the crucial role of local grain boundary structure in governing the segregation process.

To unravel the intricacies of this complex segregation behavior and to quantify the composition of the precipitates, APT was performed within the IDB region of the sample after annealing at 500 °C for 1 h. In Fig. 6 (a) and (b), 3D reconstructed volumes with isocomposition surfaces for C, Cr, and Ni are presented. The chosen isosurface values were tailored to accentuate the segregation of these elements. Our previous studies have demonstrated carbon segregation along the grain boundaries of the alloy after HPT [31]. Even more pronounced C segregation was revealed in the APT reconstruction of the annealed sample. The Cr and C isocomposition surfaces demonstrate Cr—C co-segregations at the grain boundaries. Additionally, Ni segregates separately from Cr, in agreement with STEM-EELS SI results in the DB region illustrated in Fig. 5.

The composition profile in Fig. 6 (c) along the purple arrow crossing a grain boundary reveals simultaneous Cr (peaking at ~12 at.%) and C segregation, coupled with a notable lack of Ni and Mn. Furthermore, within the grain interior, higher concentrations of Mn and Ni in comparison to those of Co and Fe affirm that the APT tip was extracted from an IDB region. In the second composition profile along the orange arrow shown in Fig. 6 (d), it is evident that Ni and Mn co-segregation occurs concurrently with the depletion of other elements, namely Fe, Co, Cr, and C. The peak concentrations of Ni and Mn reach ~31 at.% and ~ 36 at.%, while the concentration of Fe and Co is reduced to around 15 at.%. Therefore, the STEM-EELS SI, NMF and APT analyses reveal the co-segregation of Cr and C, as well as Mn and Ni, along with complex enrichment and depletion phenomena occurring at the grain boundaries in the sample annealed at 500 °C, observed in both the DB and IDB regions.

3.3.2. *Precipitation and grain growth*

Fig. 7 shows an overview of the microstructure of the sample heat-treated at 530 °C for 1 h along with corresponding elemental distributions characterized using STEM-EELS SI from the region enclosed in the white rectangle. The distinction between DB and IDB regions becomes clear in the elemental distribution maps, where the formation of numerous precipitates with varying compositions is observed. A newly formed phase, enriched in C and Cr indicating a carbide, is uniformly distributed both in the top IDB and in the bottom DB region. Additionally, the NiMn phase is also apparent across the entire analyzed region. However, the precipitates rich in Co and Fe are only present in the bottom DB region. This suggests that the formation and nucleation of the CoFe phase entail higher concentrations of Fe and Co in comparison to the nominal concentrations of the alloy constituents. This heterogeneous precipitation behavior can be attributed to the chemical inhomogeneity inherent in the as-deformed alloy after HPT processing. A more detailed analysis of the chemical composition and crystalline structure of these

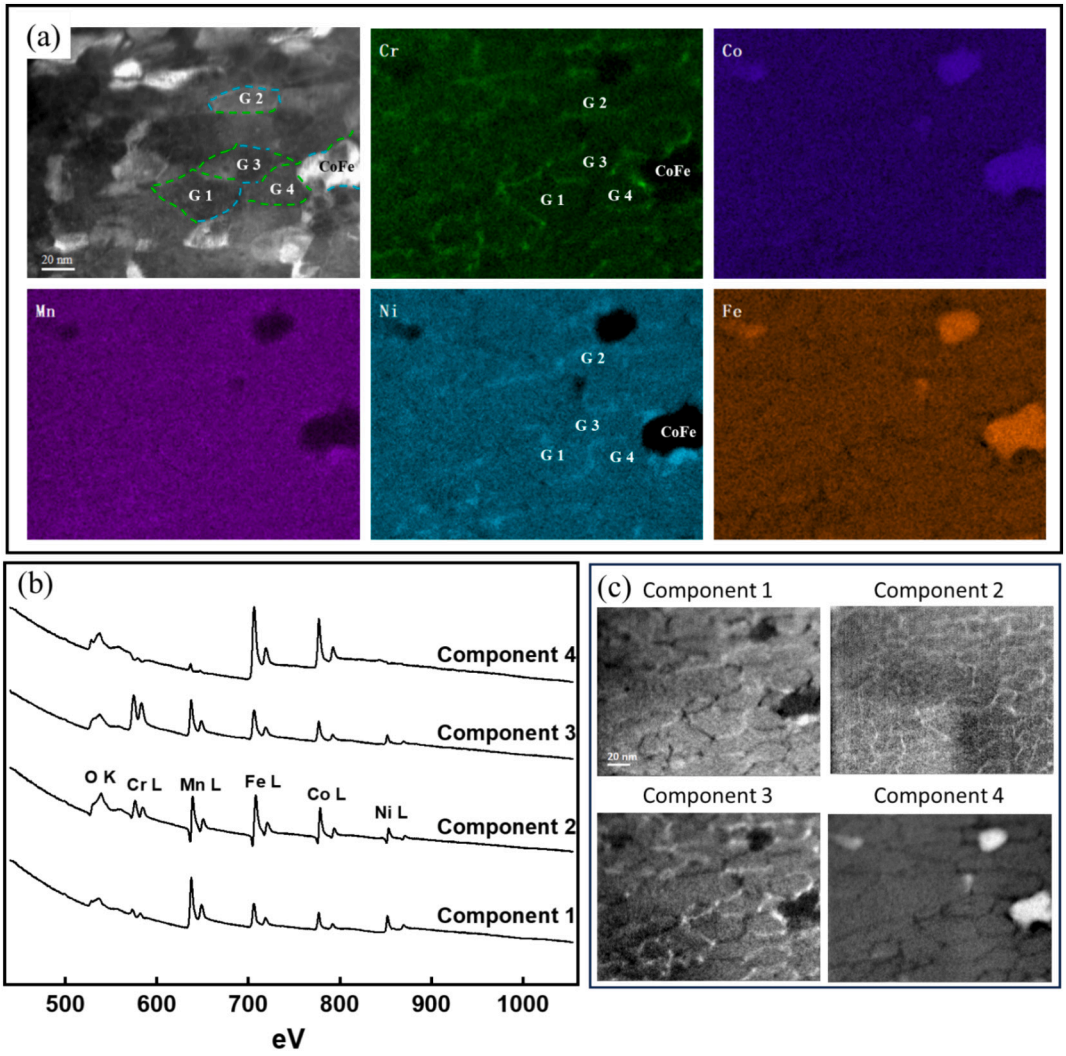

Fig. 5. The STEM-EELS SI with a step size of 0.5 nm and corresponding nonnegative matrix factorization (NMF) analysis in DB region of the sample annealed at 500 °C for 1 h. (a) The ADF image and EELS elemental maps; (b) spectra of four components extracted by NMF; (c) spatial distributions for each component.

Table 2
The calculated chemical composition of the four components from Fig. 5. (c).

Concentration in at.%	Cr	Mn	Fe	Co	Ni
Component 1	1.4	29.3	18.1	17.9	33.2
Component 2	4.7	14.6	32.6	22.5	25.3
Component 3	21.1	18.0	21.0	20.1	19.6
Component 4	0	1.3	55.1	42.9	0.6

precipitates is discussed below.

Fig. 8 provides a detailed view of the microstructure, accompanied by STEM-EELS SI elemental distribution maps, from the DB region of the sample annealed at 530 °C for 1 h. Notably, a substantial growth of the CoFe phase is discernible, exhibiting an average particle size ranging from 80 to 100 nm. The FCC-matrix grains assume an equiaxial shape with an average size ranging from 50 to 100 nm, pointing towards a significant grain growth. The EELS quantification indicates a composition of approximately 3.5 Cr, 29 Fe, 22 Co, 23 Mn, and 18 Ni (in at.%) for the FCC area in the DB region. This chemical composition reveals a distinct reduction in Cr content, which can be attributed to the formation of numerous carbides. Furthermore, a few irregularly shaped nanoprecipitates surrounding the CoFe particles, corresponding to a NiMn phase are observed (indicated by yellow arrows). Additionally, some carbides, with a larger size of approximately 50 nm, precipitated near the CoFe and NiMn phases, while others, with a smaller size ranging from 5 to 10 nm, formed at FCC grain boundaries, primarily at their junction points.

The concentration profile depicted in Fig. 8 (b), traced along the white arrow intersecting a CoFe precipitate and an FCC grain, elucidates the compositions of the involved phases and the segregation at grain boundaries. This profile illustrates the co-segregation of Mn and Ni on/near FCC grain boundaries and at the interface between FCC grains and the CoFe phase. Moreover, the elemental distribution within the FCC grains exhibits greater heterogeneity compared to the sample annealed at 500 °C. Ni and Mn not only display a strong co-segregation at the grain boundaries, but also demonstrate a noticeable enrichment in the region adjacent to the grain boundaries, as clearly observed in the Ni map. Conversely, the concentration of Co and Fe is slightly higher in the center of the FCC grains (as evident in the Co and Fe maps). This subtle inhomogeneity in the elemental distribution may be induced by thermally activated diffusion. In comparison with the DB region, the absence of the CoFe phase in the IDB region can potentially be attributed to the lower concentration of Co and Fe in these areas, as indicated in the top area of Fig.7.

To further analyze the inhomogeneous elemental distribution and precise concentration within all phases, an APT analysis was performed for the sample annealed at 530 °C for 1 h from the DB region. Fig. 9 (a) presents a 3D reconstructed volume containing several precipitated

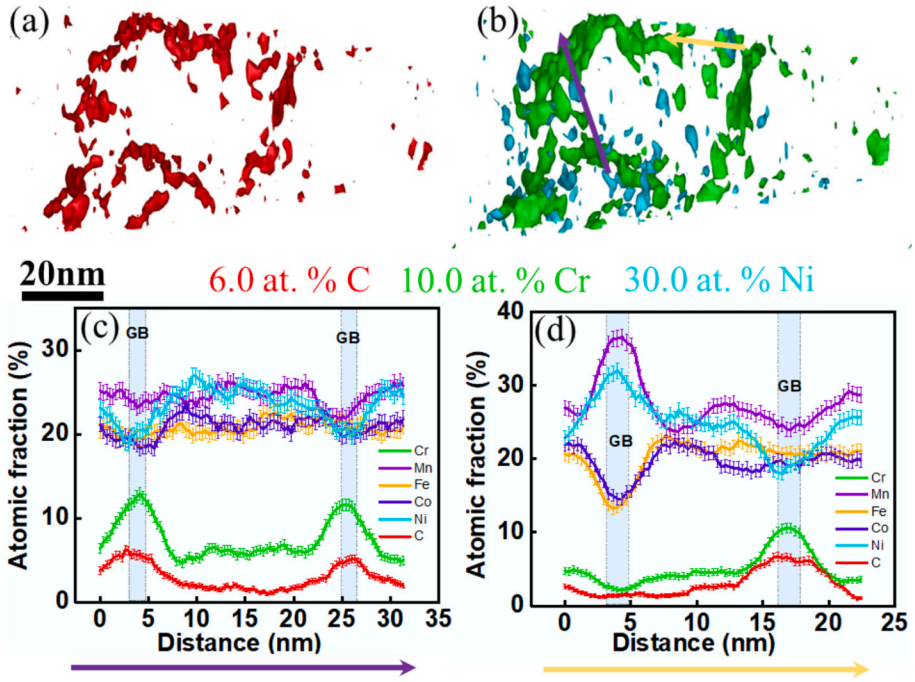

Fig. 6. APT reconstruction of the sample annealed at 500 °C showing segregation of C, Cr and Ni. (a) C 6.0 at.% isosurface, (b) Cr 10.0 at.% isosurface and Ni 30.0 at. % isosurface. Composition profiles taken along the direction indicated by the purple arrow (c) and the orange arrow (d). (For interpretation of the references to colour in this figure legend, the reader is referred to the web version of this article.)

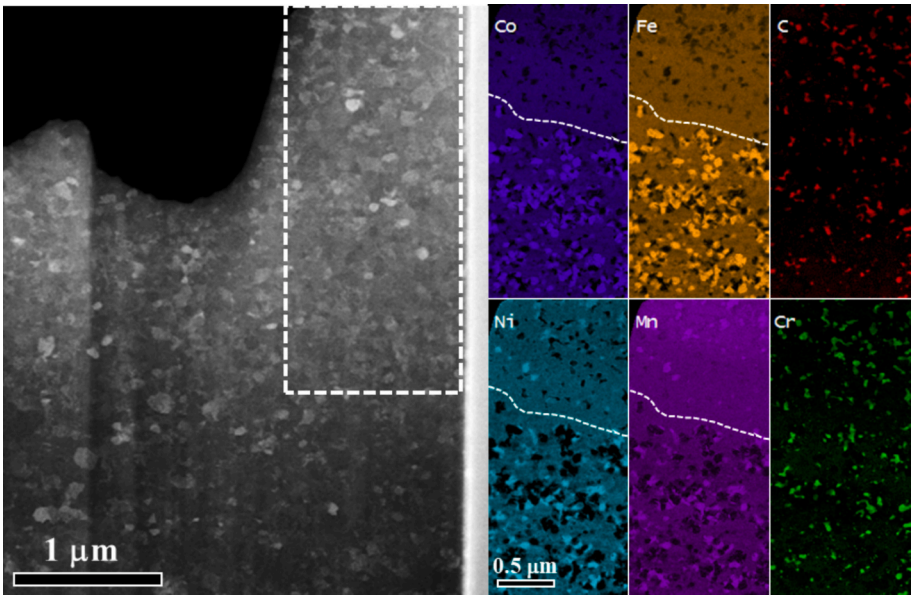

Fig. 7. ADF-STEM image and corresponding STEM-EELS SI elemental maps for all elements of the sample annealed at 530 °C for 1 h. The border between the DB (upper part of the images) and IDB regions (lower part of the images) is indicated by the white dashed line.

particles. In Fig. 9 (b), isocomposition surfaces are delineated for 55 at. % (C, Cr) in red, 75 at.% (Co, Fe) in orange, and 90 at.% (Ni, Mn). Three proximity-histograms (proxigrams) were established around the isosurface lines. Fig. 9 (c) showcases the proxigram for the 92 at.% (Ni, Mn) isosurface, revealing a high concentration of Mn and Ni in NiMn particles with a 1:1 ratio. Additionally, small amounts of Fe, Cr, and Co are present, while almost no C is detected. The proxigram centered on the 75 at.% (Co, Fe) isosurface shows roughly equal amounts of Fe and Co (both ~44 at.%), along with noticeable amounts of Ni and Mn (7.5 at.% Mn, 3.6 at.% Ni), and a small amount of C (~0.1 at.%). Similarly, the proxigram collected for the 55 at.% (C, Cr) isosurface is plotted in Fig. 9 (e). The carbide exhibits a main concentration of 24 at.% C, 52 at.% Cr, with approximately 10 at.% of Fe and Mn, small amounts of Co, and negligible Ni content, indicating a M23C6 type high-entropy carbide [32] based on the chemical composition. Table 3 displays the average composition of the FCC phase and all precipitates in the APT volume. It is evident that the concentration of Fe and Co in the FCC regions is slightly lower than that in the DB region of the as-deformed sample, indicating a significant depletion due to CoFe phase precipitation. Furthermore, a low C concentration (0.15 at.%) and a substantial reduction in Cr content within the FCC matrix suggest the precipitation of carbides.

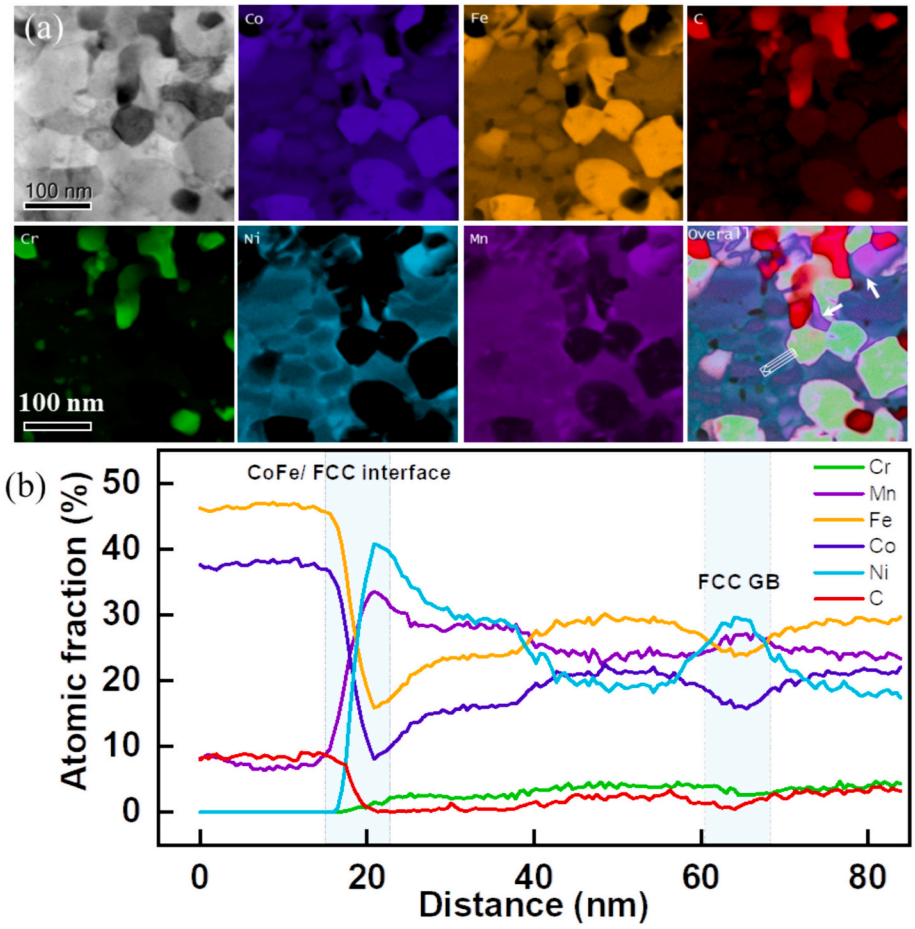

Fig. 8. (a) magnified STEM-EELS SI elemental maps of the sample annealed at 530 °C for 1 h (b) concentration profile created along the white arrow.

The microstructure and elemental distribution maps of the sample annealed at 560 °C for 1 h, obtained by means of STEM-EELS SI from the square region, are presented in Fig. 10. The white dashed lines in Mn and Co maps delineate the boundary between the IDB and DB regions, identified based on the observed precipitation behavior. Carbides enriched in Cr and C persist in their uniform distribution across all investigated areas, constituting a volume fraction of approximately 9.5 %. The mean grain size of the FCC phase is slightly increased. In the DB region, the CoFe phase is still present, exhibiting an equiaxed shape. Interestingly, NiMn is no longer observed in the IDB region, while only two NiMn particles are detected in the DB region, located near CoFe particles.

An ADF-STEM image and corresponding EELS elemental distribution maps of the sample annealed at 600 °C are shown in Fig. 11 (a). The typical equiaxial grains after recrystallization are observed in the ADF-STEM image with a mean grain size of ~200 nm. Carbides mostly precipitated at FCC-phase triple junctions between grains, alongside occasional round particles enriched in Cr, as indicated by the white circles in the Cr map. The small Cr-rich particles do not contain C marked by circles in Fig. 11 (a), suggesting that these might be Cr-rich BCC or Cr-sigma precipitates [4,7]. Moreover, some carbides contain a higher concentration of Mn in the center, which can be an indication that the carbide nuclei were Mn-rich. Additionally, it is important to note that neither the CoFe phase nor the NiMn phase exists in the sample in both DB and IDB regions. Fig. 11 (b) presents a concentration profile across a carbide and FCC grain boundaries. The carbide contains approximately 50 at.% Cr, 20 at.% Mn and 30 at.% C, indicative of a M7C3 type carbide rather than a M23C6 carbide. Furthermore, a weak segregation of Ni and Mn was observed at grain boundaries, which is less pronounced than that observed in the samples annealed at 500 and 530 °C.

3.4. *Characterization of precipitates structure*

HR-STEM images were acquired for the CoFe and the NiMn phase in the sample annealed at 530 °C. In Fig. 12 (a), an atomic resolution *Z*-contrast HAADF-STEM image of a typical CoFe phase along the [001] zone axis is presented, revealing the atom configuration corresponding to the B2 structure. This is further supported by the Fast Fourier Transform (FFT) pattern shown in Fig. 12 (d). Due to close values of atomic scattering factors of Fe and Co (3.51 for Co and 3.54 for Fe at a Bragg angle [33]), it is challenging to distinguish between atomic species based solely on diffraction contrast. However, weak blurred superlattice reflections were identified in the FFT indicated by yellow arrows. Subsequently, a nano beam electron diffraction (NBED) was collected from the CoFe phase, confirming its BCC ordered structure. Furthermore, calculations demonstrated that the lattice parameter of the B2 structure is approximately 0.293 nm, slightly larger than that of the pure binary CoFe intermetallic (ICSD 44731 cubic Im-3 m structure, a = 0.28845 nm [34]), This variation is attributed to lattice distortion induced by the presence of interstitial C atoms and substitutional Ni, Mn, and Cr atoms.

Fig. 12 (b) shows a HAADF STEM image of a NiMn precipitate. In a standard binary Mn—Ni phase diagram [35], there is a chemically ordered body-centered tetragonal (BCT) $L1_0$ structure (ICSD 104916, tetragonal P4 mmm, $a = b = 0.261$ nm, $c = 0.349$ nm [36]). However, Fig. 12 (b) suggests a structure containing multiple nanotwins, each with a width of ~10 atomic layers. The corresponding FFT in Fig. 12 (e)

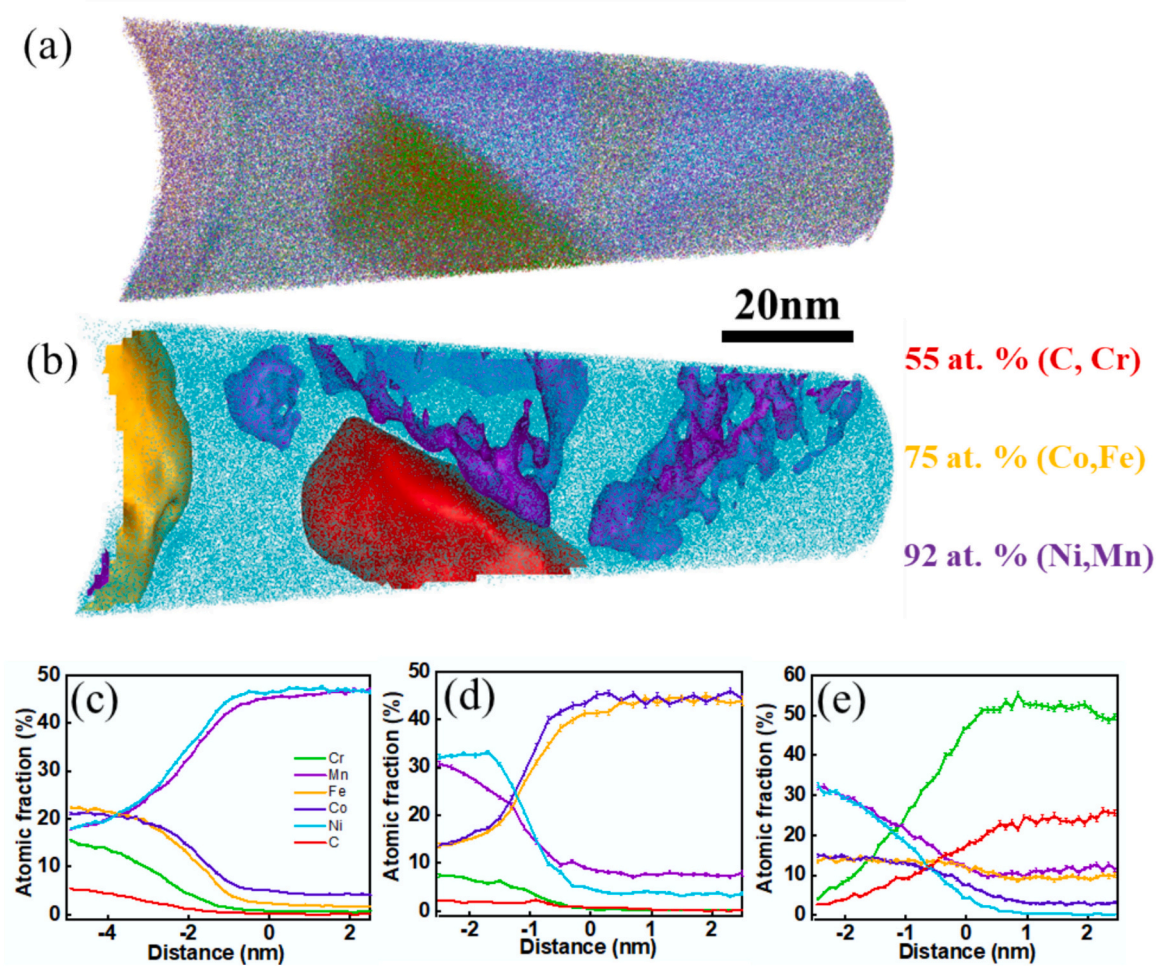

Fig. 9. (a) APT 3D reconstruction showing the overall elemental distribution in 530 °C heat-treated sample; (b) isocomposition surfaces of 55 at.% (C, Cr), 75 at.% (Co, Fe), 90 at.% (Ni, Mn); proxigrams created by the (c) NiMn surface (d), CoFe surface and (e) CCr.

Table 3
The chemical composition of all phases present in the analyzed APT volume in Fig. 9.

phase	C	Cr	Fe	Co	Mn	Ni
CoFe	0.1 ± 0.05	0.2 ± 0.05	**44.1 ± 0.7**	**44.3 ± 0.6**	7.5 ± 0.3	3.6 ± 0.2
NiMn	0.05 ± 0.02	0.6 ± 0.1	1.6 ± 0.1	4.1 ± 0.2	**46.5 ± 0.5**	**46.9 ± 0.5**
CrC	**24.4 ± 0.7**	**52.6 ± 0.8**	9.4 ± 0.5	3.1 ± 0.3	11.1 ± 0.5	0.4 ± 0.1
FCC matrix	0.15 ± 0.01	5.1 ± 0.1	23.6 ± 0.2	22.3 ± 0.2	23.7 ± 0.2	24.4 ± 0.2

indicates a twinned FCC structure without chemical ordering, which is analogous to the NBED pattern of the NiMn phase in Fig. 12 (h). The calculation of the lattice parameters ($a = b = c \approx 3.76$ Å) reveals no detectable compression of the c axis, suggesting that the NiMn phase does not correspond to the BCT $L1_0$ structure, but rather adopts a disordered FCC structure, as illustrated in Fig. 12 (i). In agreement with local HRTEM and CBED analysis above, the diffraction pattern of the 530 °C sample reveals a broader ring near the FCC (111) reflection in Fig. 3, attributed to strong overlapping of reflections of FCC matrix (111), NiMn FCC phase (111) and CoFe B2 phase (110).

Furthermore, a HRTEM image shows the Cr-rich carbide at the FCC matrix grain boundary in the sample annealed at 600 °C in Fig. 12 (c). The FFT of the carbide is shown in Fig. 12 (f) demonstrating a [221] zone axis of the M7C3 carbide. The perfect overlap of the (111) spot of the FCC grain with the (212) spots of carbide indicates that the (111) planes of the FCC are exactly parallel to the (212) plane of the carbide, as illustrated in Fig. 12 (f).

4. Discussion

In the present work, a carbon alloyed nanocrystalline FCC $Co_1Cr_{0.25}Fe_1Mn_1Ni_1$ HEA was isochronally annealed at a series of temperatures. At low annealing temperatures (200–400 °C), a microstructure of the alloy was stable, as neither a grain growth of the FCC matrix phase, nor a precipitation of any secondary phases were detected. The results of the comprehensive microstructural analysis of samples annealed in a temperature range of 500–600 °C illustrate a decomposition of the nanocrystalline single-phase solid solution leading to grain boundary segregation and new phases precipitating during annealing. The annealing temperature ranges where particular phases are stable are shown in Fig. 13 and compared with the literature data for the equiatomic CoCrFeMnNi (Cantor) alloy [3,4,7,37–40]. Let us note that due to the initial chemical inhomogeneity of the alloy and the presence of Ni, Mn rich IDB regions and Co, Fe rich DB regions (Fig. 2 and Table 1), there was some difference in the preferential location of precipitated phases. As will be discussed below, we believe that this difference is mostly related to a limited diffusion of particular elements at certain temperatures and relatively short annealing time (1 h). Most likely, after long-term annealing, a homogeneous distribution of phases would be obtained. In the following subsections, segregation behavior and the precipitated phases will be discussed with regard to the literature data.

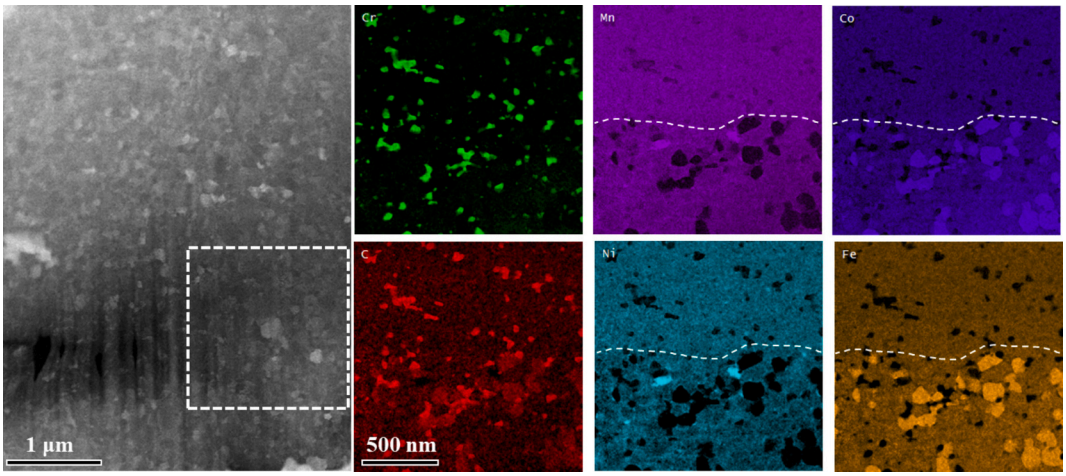

Fig. 10. ADF-STEM image and corresponding STEM-EELS SI elemental maps for all elements of the sample annealed at 530 °C for 1 h. The board of DB and IDB regions are indicated by the white dashed line.

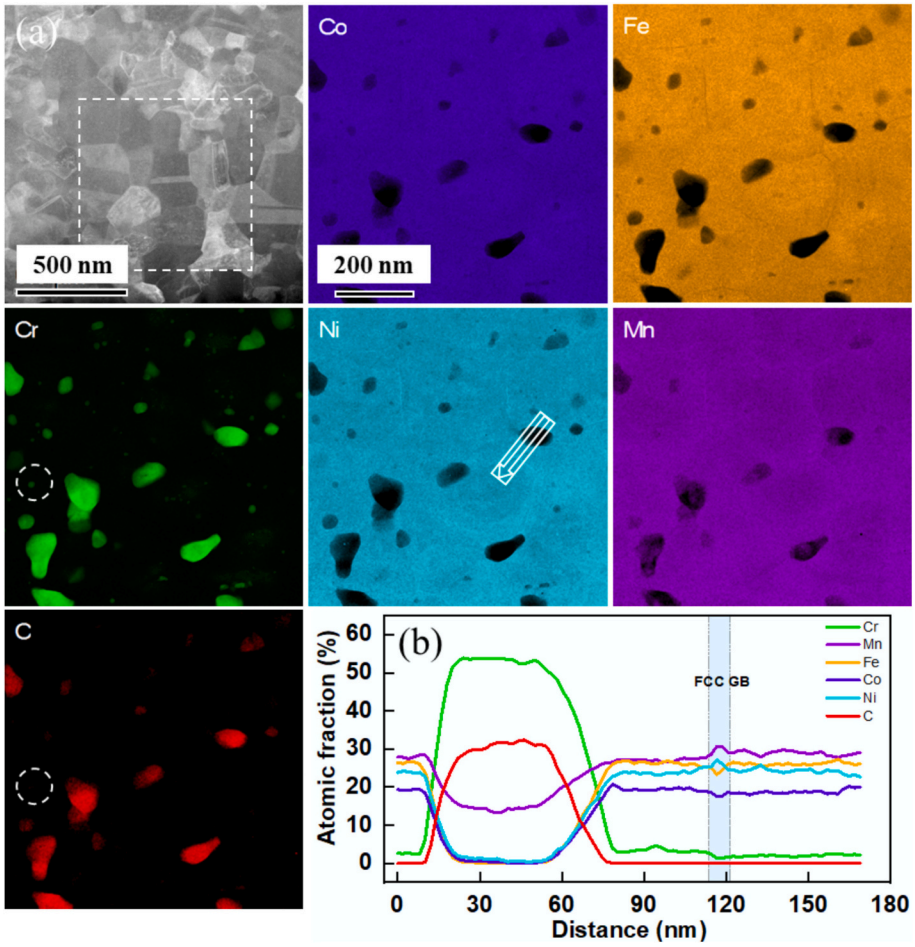

Fig. 11. (a) STEM-ELLS elemental maps for all constitutive elements and corresponding ADF image for a sample annealed at 600 °C for 1 h; (b) a concentration profile along the white arrow. White circles indicate the Cr enriched particles.

4.1. Elemental segregations

As discussed in our previous work [31], grain boundary segregations of carbon were found in this alloy after HPT deformation. The present investigation revealed that after annealing at 500 °C for 1 h these carbon segregations became more pronounced, and additionally Cr, Ni and Mn segregated at the grain boundaries, as shown in Fig. 4. Interestingly, an elemental partitioning was clearly observed as Ni and Mn segregated together and separately from C and Cr. Li et al. have systematically studied grain boundary segregations in coarse-grained equiatomic Cantor alloy during annealing at 450 °C by means of APT [41]. They clearly demonstrated a partitioning of segregated elements when Fe, Co

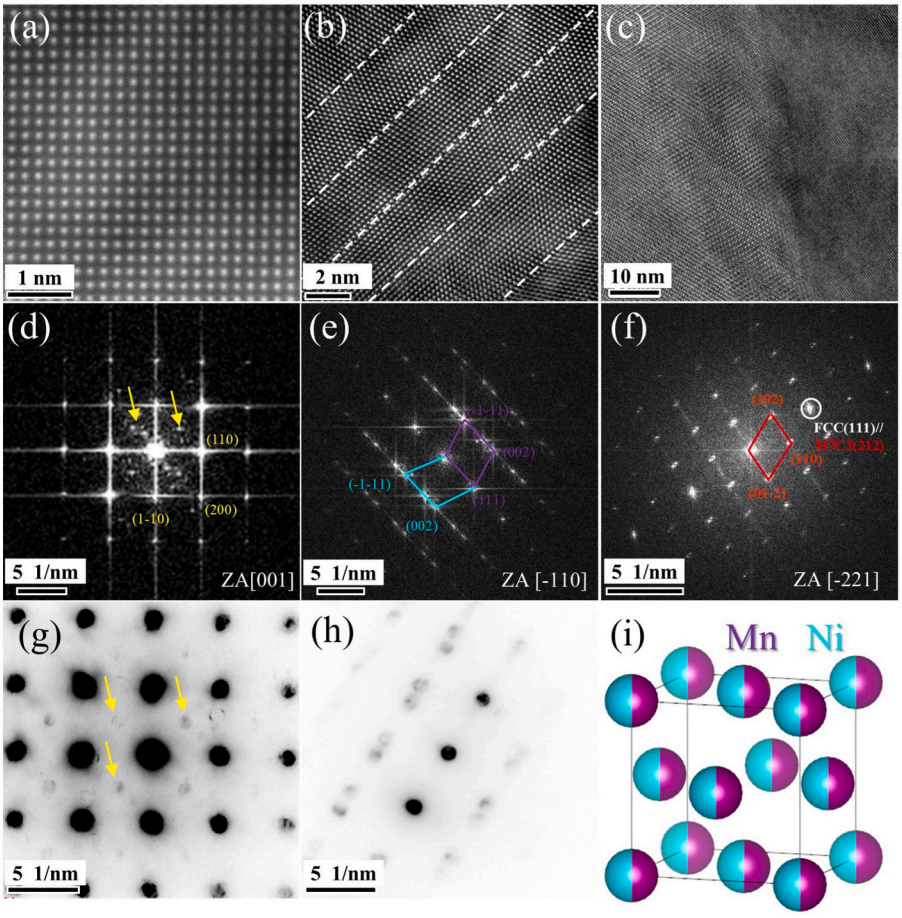

Fig. 12. HRSTEM images of the (a) CoFe phase, (b) NiMn phase and (c) HRTEM image of a carbide on the FCC grain boundary; (d) FFT of (a) indexed to be [001] zone axis; (e) FFT of (b) indexed to be [−110] zone axis based on FCC structure; (f) FFT of (c) indexed to be [−221] zone axis of a M7C3 carbide; (g) and (h) are the NBED of (a) and (b); (i) shows the disordered NiMn FCC structure.

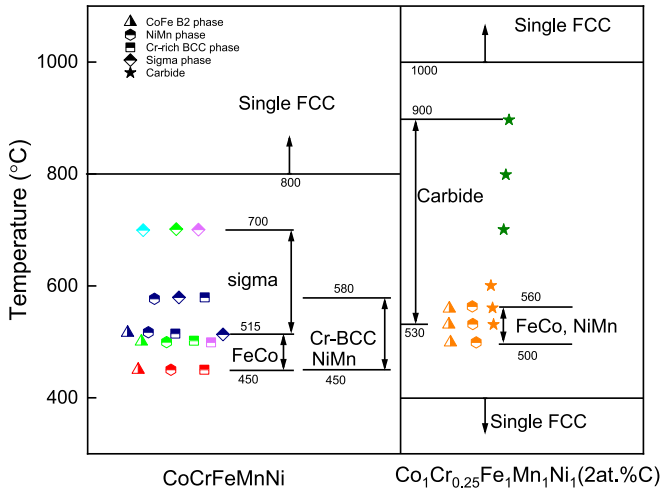

Fig. 13. Temperature ranges of various phases precipitation in CoCrFeMnNi and our experimental alloy.

and Cr fluctuated periodically in antiphase with Ni and Mn in the same grain boundary plane. In particular, compositional fluctuations occurred with a wavelength of ~6–10 nm and with an amplitude of ~5–7 at.%. Similar results were obtained in the non-equiatomic nanocrystalline CoCuFeMnNi alloy with a mean grain size of ~100 nm, where Cu, Ni and Co segregate separately within a single GB at a low annealing temperature of 250 °C [28]. In our case of a nanocrystalline alloy with a grain size of 20 nm, the length of a grain boundary segment is comparable with the compositional fluctuations wavelength found in [41] (or even smaller than that), which is why different atomic species decorate neighboring grain boundary segments. It had been proposed in [41] that such a peculiar segregation behavior results from a spinodal decomposition along grain boundaries in a similar way as it was previously observed in a Fe—Mn alloy [42]. Generally, bulk spinodal decomposition phenomena are very common in Fe-Ni-Mn, Fe-Co-Cr and Fe—Cr alloys [43–46] as well as in many HEAs [47–51] and are related to a miscibility gap in these alloy systems at particular temperatures and concentrations. Li et al. argued that in the framework of classical alloy thermodynamics, segregation of atoms is energetically favorable as it leads to a decrease in the grain boundary free energy [41]. Indeed, prior experimental and theoretical investigations have observed a reduction in the Gibbs free energy of grain boundaries (GBs) through the segregation of Ni, Mn, or Cr in Fe-based alloys [52–55]. Then, when the local concentration of segregated atoms becomes higher than the miscibility gap, decomposition of the solid solution facilitated by enhanced diffusion in grain boundaries may occur. We would like to highlight that Li et al. found that Cr segregations were less pronounced in comparison with Mn and Ni ones in the annealed equiatomic Cantor alloy, whereas in our case Cr segregations were quite strong and the atomic concentration of Cr was similar to that of Ni and Mn (Fig. 4). We explain it by a relatively high carbon concentration in grain boundaries and the strong affinity of Cr to carbon.

Moreover, Zhou et al. and Chen et al. reported that the spatial distribution of elements during the formation of chemical short-range order

in CrCoNi and VCoNi alloys is strongly depended on their spatial correlation coefficient, which can be quantified by the following equation [56,57]:$C_{A\ B}(r) = \frac{\langle (x_A(0) \ \langle x_A \rangle)(x_B(r) \ \langle x_B \rangle) \rangle}{\sqrt{\langle (x_A \ \langle x_A \rangle)^2 \rangle}\sqrt{\langle (x_B \ \langle x_B \rangle)^2 \rangle}}$, where x_A (0) is the atomic concentration of element A at reference position (0) and x_B (r) is the concentration of B a distance of r away, and $\langle x_A \rangle$ and $\langle x_B \rangle$ are the average chemical composition of A and B, respectively. In the CrCoNi alloy, the calculated values of $C_{Cr\text{-}Ni}$, $C_{Co\text{-}Ni}$ and $C_{Cr\text{-}Co}$ are all negative at both 600 and 1000 °C, indicating that like elements tend to avoid becoming nearest neighbors. The quantitative analysis aligns well with our observations, where two distinct types of grain boundaries decorated by C—Cr and Ni—Mn co-segregations are distributed at specific grain boundaries on a scale of tens of nanometers. Therefore, we attribute this anti-segregation behavior, particularly between Cr and Ni, to the intrinsic negative formation energy of their compounds [57] and the degree of spatial correlation between the elements. Similar correlation-based evaluations could potentially be applied in future studies to further understand co-segregation behavior.

4.2. Precipitation

Different kinds of secondary phases precipitated in the nanocrystalline $Co_1Cr_{0.25}Fe_1Mn_1Ni_1$ (2 at.% C) alloy during one hour annealing in the temperature range between 500 and 600 °C (Fig. 13).

4.2.1. CoFe B2 phase

This phase was observed in samples annealed at 500, 530 and 560 °C and was absent after annealing at 600 °C. The mean size of CoFe particles was the same as that of the FCC phase at the respective annealing temperature. CoFe was detected only in DB regions, i.e. in regions with higher Co and Fe content (Table 1). CoFe B2 phase was also found in homogenized Cantor alloy in both coarse [3,4] and nano-grained [7] states after long annealing in a temperature range from 450 to 515 °C (Fig. 13). The reasons why CoFe particles did not form in the IDB regions in the present investigation are not clear. The difference in atomic concentrations of both elements in the IDB regions (~20 at.% of Co and 17 at.% of Fe, Table 1) and in the homogenized Cantor alloy (~ 20 at.% of both Co and Fe) is negligible. Most likely, a different precipitation behavior of this phase in the DB and IDB regions might be related to the slow diffusion of both elements at temperatures <600 °C. Indeed, in coarse-grained Cantor alloy CoFe phase was observed after annealing for 500 h [3,4], and in nanocrystalline alloy after 15 h [7]. In our case, the CoFe phase precipitated after annealing for one hour in DB region with higher atomic concentrations of Co and Fe (Table 1), which means that the diffusion path was shorter. Bulk diffusion coefficients were determined for all constituting elements in the equiatomic Cantor alloy in a wide temperature range down to 650 °C in [58]. Extrapolating data of [58], one can estimate that at 500–560 °C the mean diffusion path of both Co and Fe atoms is $l = \sqrt{Dt} = \left(\sqrt{5 \times 10^{-21} \times 3600}\right) = 4.2$ nm during one hour, that is much less than a mean CoFe particle size of 100 nm (Fig. 8). Even taking into account that diffusion is accelerated in the presence of a high density of grain boundaries and with the addition of interstitial C atoms [59], it seems that this acceleration is not sufficient for the precipitation of CoFe particles in the IDB regions. A strong enrichment with Ni and Mn is observed at the interphase boundary between CoFe and FCC in Fig. 8 (b) (with a concentration much higher than in the GB segregation in the right part of the same figure). Most likely, this results from the uphill diffusion of the excess Ni and Mn atoms to the interphase boundary due to the formation of CoFe particle.

4.2.2. NiMn phase

A NiMn phase with a disordered FCC structure (or its precursor) with a size of a few nanometers precipitated along the triple junctions and grain boundaries in the IDB region after annealing at 500 °C, and in both regions after annealing at 530 °C (Figs. 4 and 6). After annealing at 560 °C, quite a few large NiMn particles were present apparently only in the DB region (Fig. 10). As a bulk diffusion of Ni and Mn is very slow in the temperature range between 500 °C and 560 °C similarly to that of the other constituting alloy elements [58], most likely, NiMn phase nucleation was facilitated by segregation of Ni and Mn at grain boundaries. After annealing at 530 and 560 °C, the size of NiMn particles was comparable with the grain size of the FCC phase. A $L1_0$ structured NiMn phase was found in a coarse-grained Cantor alloy after long-term annealing in a temperature range from 500 to 580 °C [3,4]. However, in the nanocrystalline Cantor alloy, the NiMn phase had been identified after annealing at 450 °C as a disordered FCC phase [7], in agreement with our results. Therefore, both CoFe and NiMn phases co-exist in the same temperature range in the Cr-reduced carbon alloyed Cantor type alloy (Fig. 13).

4.2.3. Cr-rich carbide phase

Cr-rich carbides of M7C3 type were observed in the present investigation at annealing temperatures of 530 °C and higher (Fig. 4). This is distinct from the equiatomic Cantor alloy, where the Cr-rich BCC phase is formed during the annealing in a range from 450 to 580 °C, and the Cr-enriched σ phase precipitated over a wide temperature range from 515 to 700 °C [3]. In the nanocrystalline Cantor alloy produced by HPT only Cr-rich particles were observed after annealing at 450 °C [7]. This difference in precipitation behavior can be explained by the presence of carbon in our experimental alloy. Cr has a great affinity to carbon, which makes the formation of carbides energetically more favorable than the formation of σ phase. For example, the enthalpy of Cr7C3 formation is strongly negative (approx. -150 kJ/mol) [60] and that of the CrFe sigma phase is positive (~2.7 kJ/mol) [61]. Yet, tiny Cr-rich granules were also detected in the grain interior of the alloy annealed at 600 °C, as illustrated in Fig. 11, which could be a Cr-rich BCC phase according to the composition analysis. The temperature range for carbide formation in the present alloy has been reported from 530 °C to 900 °C [40], whereas at temperatures above 1000 °C, a single FCC solid solution forms, which is about 200 °C higher than in the Cantor alloy (Fig. 13).

5. Conclusions

A carbon-doped, non-equiatomic nanocrystalline CoCrFeMnNi high-entropy alloy (HEA) was synthesized via high-pressure torsion (HPT) and subsequently subjected to isochronal annealing in the temperature range of 200 to 600 °C for one hour. The microstructure evolution was characterized and analyzed. The main findings can be summarized as follows:

1. Grain boundary segregation of Ni, Mn and Cr was observed in the sample after annealing at 500 °C for 1 h as well as an increase in carbon segregation concentration compared to the as-deformed state. Ni and Mn co-segregate in some GB segments, whereas Cr and C co-segregate in other GB segments. This is explained by the spinodal decomposition in the grain boundary areas and the strong chemical affinity of Cr to carbon. The anti-segregation behavior, particularly between Cr and Ni, is attributed to the degree of spatial correlation between the elements.
2. Precipitation of ordered CoFe (B2) and disordered NiMn (FCC) phases occurred during annealing between 500 and 560 °C. The formation of these phases was influenced by local elemental concentrations, with precipitation of NiMn and CoFe phases observed when the concentrations exceeded approximately 30–35 at.% for NiMn and more than 25 at.% for CoFe. The precipitation of NiMn was primarily associated with GB segregation of Ni and Mn, while CoFe precipitation was linked to initial compositional inhomogeneities in the alloy. Additionally, Cr-rich M7C3 carbides began to precipitate at annealing temperatures above 530 °C and remained beyond 600 °C.
3. The initial grain size of the FCC phase (~20 nm) was stable up to 500 °C. Moderate grain growth occurred between 530 and 560 °C. In

this temperature range, the microstructure consisted of FCC grains, NiMn, CoFe and carbide particles with a similar size. At 600 °C, in the absence of NiMn and CoFe precipitates, significant grain growth of the FCC phase to approximately 280 nm was observed.

CRediT authorship contribution statement

Yemao Lu: Writing – review & editing, Writing – original draft, Investigation, Formal analysis, Data curation. **Sangjun Kang:** Writing – review & editing, Formal analysis. **Gennadiy Salishchev:** Writing – review & editing, Resources. **Anastasia Semenjuk:** Writing – review & editing, Resources. **Xiang Chen:** Writing – review & editing. **Christian Kübel:** Writing – review & editing, Supervision. **Horst Hahn:** Writing – review & editing, Supervision. **Yulia Ivanisenko:** Writing – review & editing, Writing – original draft, Supervision, Conceptualization.

Declaration of competing interest

The authors declare that they have no known competing financial interests or personal relationships that could have appeared to influence the work reported in this paper.

Acknowledgements

Y.L. acknowledges the funding support provided by China Scholarship Council (CSC). This work was partly carried out with the support of the Karlsruhe Nano-Micro Facility (KNMFi, www.knmf.kit.edu), a Helmholtz Research Infrastructure at Karlsruhe Institute of Technology. G.S. and A.S. are grateful for the financial support by the Russian Science Foundation (Agreement No. 19-79-30066).

Data availability

Data will be made available on request.

References

[1] B. Cantor, I.T.H. Chang, P. Knight, A.J.B. Vincent, Microstructural development in equiatomic multicomponent alloys, Mater. Sci. Eng. A 375–377 (1–2 SPEC. ISS) (2004) 213–218.
[2] J.W. Yeh, S.K. Chen, S.J. Lin, J.Y. Gan, T.S. Chin, T.T. Shun, C.H. Tsau, S.Y. Chang, Nanostructured high-entropy alloys with multiple principal elements: novel alloy design concepts and outcomes, Adv. Eng. Mater. 6 (5) (2004) 299–303.
[3] K.H. Lee, S.K. Hong, S.I. Hong, Precipitation and decomposition in CoCrFeMnNi high entropy alloy at intermediate temperatures under creep conditions, Materialia 8 (June) (2019).
[4] F. Otto, A. Dlouhý, K.G. Pradeep, M. Kuběnová, D. Raabe, G. Eggeler, E.P. George, Decomposition of the single-phase high-entropy alloy CrMnFeCoNi after prolonged anneals at intermediate temperatures, Acta Mater. 112 (2016) 40–52.
[5] M. Vaidya, A. Karati, A. Marshal, K.G. Pradeep, B.S. Murty, Phase evolution and stability of nanocrystalline CoCrFeNi and CoCrFeMnNi high entropy alloys, J. Alloys Compd. 770 (2019) 1004–1015.
[6] G. Laplanche, S. Berglund, C. Reinhart, A. Kostka, F. Fox, E.P. George, Phase stability and kinetics of σ-phase precipitation in CrMnFeCoNi high-entropy alloys, Acta Mater. 161 (2018) 338–351.
[7] B. Schuh, F. Mendez-Martin, B. Völker, E.P. George, H. Clemens, R. Pippan, A. Hohenwarter, Mechanical properties, microstructure and thermal stability of a nanocrystalline CoCrFeMnNi high-entropy alloy after severe plastic deformation, Acta Mater. 96 (2015) 258–268.
[8] N.D. Stepanov, N.Y. Yurchenko, M.A. Tikhonovsky, G.A. Salishchev, Effect of carbon content and annealing on structure and hardness of the CoCrFeNiMn-based high entropy alloys, J. Alloys Compd. 687 (2016) 59–71.
[9] J.Y. Ko, S.I. Hong, Microstructural evolution and mechanical performance of carbon-containing CoCrFeMnNi-C high entropy alloys, J. Alloys Compd. 743 (2018) 115–125.
[10] L.B. Chen, R. Wei, K. Tang, J. Zhang, F. Jiang, L. He, J. Sun, Heavy carbon alloyed FCC-structured high entropy alloy with excellent combination of strength and ductility, Mat. Sci. Eng. a-Struct. 716 (January) (2018) 150–156.
[11] L. Guo, X. Ou, S. Ni, Y. Liu, M. Song, Effects of carbon on the microstructures and mechanical properties of FeCoCrNiMn high entropy alloys, Mater. Sci. Eng. A 746 (December 2018) (2019) 356–362.
[12] M.Y. He, Y.F. Shen, N. Jia, P.K. Liaw, C and N doping in high-entropy alloys: a pathway to achieve desired strength-ductility synergy, Appl. Mater. Today 25 (2021) 101162.
[13] M. Vaghari, K. Dehghani, The effect of carbon on the microstructures and mechanical properties of non-equiatomic Cr15Cu5Fe20Mn25Ni35 high-entropy alloy, Mater. Sci. Eng. A 919 (2025) 147525.
[14] Z. Li, Interstitial equiatomic CoCrFeMnNi high-entropy alloys: carbon content, microstructure, and compositional homogeneity effects on deformation behavior, Acta Mater. 164 (November) (2019) 400–412.
[15] Z. Wu, C.M. Parish, H. Bei, Nano-twin mediated plasticity in carbon-containing FeNiCoCrMn high entropy alloys, J. Alloys Compd. 647 (2015) 815–822.
[16] S.V. Astafurov, E.V. Melnikov, K.A. Reunova, M.Y. Panchenko, E.A. Zagibalova, K. V. Krukovskii, E.G. Astafurova, The way to improve strength and ductility of heavily carbon-alloyed high-entropy Fe20Mn20Cr20Ni20Co15C5 alloy, Mater. Sci. Eng. A 851 (2022) 143628.
[17] F.D.C. Garcia Filho, R.O. Ritchie, M.A. Meyers, S.N. Monteiro, Cantor-derived medium-entropy alloys: bridging the gap between traditional metallic and high-entropy alloys, J. Mater. Res. Technol. 17 (2022) 1868–1895.
[18] H. Shahmir, J. He, Z. Lu, M. Kawasaki, T.G. Langdon, Effect of annealing on mechanical properties of a nanocrystalline CoCrFeNiMn high-entropy alloy processed by high-pressure torsion, Mater. Sci. Eng. A 676 (2016) 294–303.
[19] A. Heczel, M. Kawasaki, J.L. Lábár, J.I. Jang, T.G. Langdon, J. Gubicza, Defect structure and hardness in nanocrystalline CoCrFeMnNi high-entropy alloy processed by high-pressure torsion, J. Alloys Compd. 711 (2017) 143–154.
[20] Y. Lu, A. Mazilkin, T. Boll, N. Stepanov, S. Zherebtzov, G. Salishchev, É. Ódor, T. Ungar, E. Lavernia, H. Hahn, Y. Ivanisenko, Influence of carbon on the mechanical behavior and microstructure evolution of CoCrFeMnNi processed by high pressure torsion, Materialia 16 (March) (2021) 101059.
[21] A. Bachmaier, R. Pippan, O. Renk, Effect of carbon in severe plastically deformed metals, Adv. Eng. Mater. 22 (12) (2020).
[22] Y. Ivanisenko, X. Sauvage, A. Mazilkin, A. Kilmametov, J.A. Beach, B.B. Straumal, Bulk nanocrystalline ferrite stabilized through grain boundary carbon segregation, Adv. Eng. Mater. 20 (10) (2018) 1–6.
[23] X. Sauvage, G. Wilde, S.V.V. Divinski, Z. Horita, R.Z.Z. Valiev, Grain boundaries in ultrafine grained materials processed by severe plastic deformation and related phenomena, Mater. Sci. Eng. A 540 (2012) 1–12.
[24] L. Han, F. Maccari, I.R. Souza Filho, N.J. Peter, Y. Wei, B. Gault, O. Gutfleisch, Z. Li, D. Raabe, A mechanically strong and ductile soft magnet with extremely low coercivity, Nature 608 (7922) (2022) 310–316.
[25] Y. Xiao, Y. Li, A. Kostka, M. Rajkowski, M. Schneider, G. Eggeler, G. Laplanche, Annealing-induced hardening in single-phase FCC, equiatomic CrCoNi and non-equiatomic CrCoNiMo medium-entropy alloys, J. Mater. Res. Technol. 30 (2024) 4762–4776.
[26] S. Ma, W. Liu, Q. Li, J. Zhang, S. Huang, Y. Xiong, B. Xu, T. Yang, S. Zhao, Mechanism of elemental segregation around extended defects in high-entropy alloys and its effect on mechanical properties, Acta Mater. 264 (2024).
[27] M.V. Klimova, A.O. Semenyuk, D.G. Shaysultanov, G.A. Salishchev, S. V. Zherebtsov, N.D. Stepanov, Effect of carbon on cryogenic tensile behavior of CoCrFeMnNi-type high entropy alloys, J. Alloys Compd. 811 (2019) 152000.
[28] L.S. Mantha, B.E. MacDonald, X. Mu, A. Mazilkin, J. Ivanisenko, H. Hahn, E. J. Lavernia, S. Katnagallu, C. Kübel, Grain boundary segregation induced precipitation in a non equiatomic nanocrystalline CoCuFeMnNi compositionally complex alloy, Acta Mater. 220 (2021) 117281.
[29] C. Gammer, C. Mangler, C. Rentenberger, H.P. Karnthaler, Quantitative local profile analysis of nanomaterials by electron diffraction, Scr. Mater. 63 (3) (2010) 312–315.
[30] T.M. Smith, M.S. Hooshmand, B.D. Esser, F. Otto, D.W. McComb, E.P. George, M. Ghazisaeidi, M.J. Mills, Atomic-scale characterization and modeling of 60°dislocations in a high-entropy alloy, Acta Mater. 110 (2016) 352–363.
[31] Y. Lu, H. Hahn, Y. Ivanisenko, Carbon segregation in CoCrFeMnNi high-entropy alloy driven by high-pressure torsion at room and cryogenic temperatures, Adv. Eng. Mater. 25 (9) (2023) 2201473.
[32] E. Castle, T. Csanádi, S. Grasso, J. Dusza, M. Reece, Processing and properties of high-entropy ultra-high temperature carbides, Sci. Rep. 8 (1) (2018) 1–12.
[33] C.B.C. David, B. Williams, Transmission Electron Microscopy:A Textbook for Materials Science, Springer, 2009.
[34] P. Bayliss, Revised unit-cell dimensions, space group, and chemical formula of some metallic minerals, Can. Mineral. 28 (4) (1990) 751–755.
[35] H. Okamoto, Mn-Ni (Manganese-Nickel), J. Phase Equilib. Diffus. 28 (4) (2007) 406–407.
[36] V.E. Egorushkin, S.N. Kulkov, S.E. Kulkova, Electronic structure and the theory of phase transformations in NiMn, Physica B+C 123 (1) (1983) 61–68.
[37] F. Ye, Z. Jiao, Y. Yuan, Precipitation behaviors and properties of micro-beam plasma arc cladded CoCrFeMnNi high-entropy alloy at elevated temperatures, Mater. Chem. Phys. 236 (July) (2019) 121801.
[38] K. Cho, Y. Fujioka, T. Nagase, H.Y. Yasuda, Grain refinement of non-equiatomic Cr- rich CoCrFeMnNi high-entropy alloys through combination of cold rolling and precipitation of σ phase, Mater. Sci. Eng. A 735 (May) (2018) 191–200.
[39] X. Zhu, X. Zhou, S. Yu, C. Wei, J. Xu, Y. Wang, Effects of annealing on the microstructure and magnetic property of the mechanically alloyed FeSiBAlNiM (M=Co, Cu, Ag) amorphous high entropy alloys, J. Magn. Magn. Mater. 430 (January) (2017) 59–64.
[40] M. Klimova, D. Shaysultanov, A. Semenyuk, S. Zherebtsov, N. Stepanov, Effect of carbon on recrystallised microstructures and properties of CoCrFeMnNi-type high-entropy alloys, J. Alloys Compd. 851 (2021) 156839.
[41] L. Li, Z. Li, A. Kwiatkowski da Silva, Z. Peng, H. Zhao, B. Gault, D. Raabe, Segregation-driven grain boundary spinodal decomposition as a pathway for phase nucleation in a high-entropy alloy, Acta Mater. 178 (2019) 1–9.

[42] A. Kwiatkowski Da Silva, D. Ponge, Z. Peng, G. Inden, Y. Lu, A. Breen, B. Gault, D. Raabe, Phase nucleation through confined spinodal fluctuations at crystal defects evidenced in Fe-Mn alloys, Nat. Commun. 9 (1) (2018).
[43] W.K. Choo, J.H. Kim, J.C. Yoon, Microstructural change in austenitic Fe-30.0wt% Mn-7.8wt%Al-1.3wt%C initiated by spinodal decomposition and its influence on mechanical properties, Acta Mater. 45 (12) (1997) 4877–4885.
[44] M.K. Miller, J.M. Hyde, M.G. Hetherington, A. Cerezo, G.D.W. Smith, C.M. Elliott, Spinodal decomposition in Fe-Cr alloys: experimental study at the atomic level and comparison with computer models—I. Introduction and methodology, Acta Metall. Mater. 43 (9) (1995) 3385–3401.
[45] J. Singh, C.M. Wayman, Age-hardening characteristics of a martensitic FeNiMn alloy, Mater. Sci. Eng. 94 (1987) 233–242.
[46] F. Zhu, P. Haasen, R. Wagner, An atom probe study of the decomposition of FeCrCo permanent magnet alloys, Acta Metall. 34 (3) (1986) 457–463.
[47] Y.J. Liang, L. Wang, Y. Wen, B. Cheng, Q. Wu, T. Cao, Q. Xiao, Y. Xue, G. Sha, Y. Wang, Y. Ren, X. Li, L. Wang, F. Wang, H. Cai, High-content ductile coherent nanoprecipitates achieve ultrastrong high-entropy alloys, Nat. Commun. 9 (1) (2018).
[48] A. Manzoni, H. Daoud, R. Völkl, U. Glatzel, N. Wanderka, Phase separation in equiatomic AlCoCrFeNi high-entropy alloy, Ultramicroscopy 132 (2013) 212–215.
[49] C.-J. Tong, Y.-L. Chen, J.-W. Yeh, S.-J. Lin, S.-K. Chen, T.-T. Shun, C.-H. Tsau, S.-Y. Chang, Microstructure characterization of Alx CoCrCuFeNi high-entropy alloy system with multiprincipal elements, Metall. Mater. Trans. A 36 (4) (2005) 881–893.
[50] L.J. Santodonato, Y. Zhang, M. Feygenson, C.M. Parish, M.C. Gao, R.J.K. Weber, J. C. Neuefeind, Z. Tang, P.K. Liaw, Deviation from high-entropy configurations in the atomic distributions of a multi-principal-element alloy, Nat. Commun. 6 (2015) 1–13.
[51] J.A. Hanna, I. Baker, M.W. Wittmann, P.R. Munroe, A new high-strength spinodal alloy, J. Mater. Res. 20 (4) (2005) 791–795.
[52] E.D. Hondros, M.P. Seah, The theory of grain boundary segregation in terms of surface adsorption analogues, Metall. Trans. A. 8 (9) (1977) 1363–1371.
[53] M. Guttmann, Equilibrium segregation in a ternary solution: a model for temper embrittlement, Surf. Sci. 53 (1) (1975) 213–227.
[54] P. Gas, M. Guttmann, J. Bernardini, The interactive co-segregation of Sb and Ni at the grain boundaries of ultra-high purity Fe-base alloys, Acta Metall. 30 (7) (1982) 1309–1316.
[55] P. Lejcek, Grain Boundary Segregation in Metals, Springer Science & Business Media, 2010.
[56] X. Chen, Q. Wang, Z. Cheng, M. Zhu, H. Zhou, P. Jiang, L. Zhou, Q. Xue, F. Yuan, J. Zhu, X. Wu, E. Ma, Direct observation of chemical short-range order in a medium-entropy alloy, Nature 592 (7856) (2021) 712–716.
[57] L. Zhou, Q. Wang, J. Wang, X. Chen, P. Jiang, H. Zhou, F. Yuan, X. Wu, Z. Cheng, E. Ma, Atomic-scale evidence of chemical short-range order in CrCoNi medium-entropy alloy, Acta Mater. 224 (2022).
[58] D. Gaertner, J. Kottke, Y. Chumlyakov, F. Hergemöller, G. Wilde, S.V. Divinski, Tracer diffusion in single crystalline CoCrFeNi and CoCrFeMnNi high-entropy alloys: kinetic hints towards a low-temperature phase instability of the solid-solution? Scr. Mater. 187 (2020) 57–62.
[59] O.A. Lukianova, Z. Rao, V. Kulitckii, Z. Li, G. Wilde, S.V. Divinski, Impact of interstitial carbon on self-diffusion in CoCrFeMnNi high entropy alloys, Scr. Mater. 188 (2020) 264–268.
[60] S. Anthonysamy, K. Ananthasivan, I. Kaliappan, V. Chandramouli, P.R. Vasudeva Rao, C.K. Mathews, K.T. Jacob, S. Anthonysamy, K. Ananthasivan, I. Kaliappan, V. Chandramouli, Gibbs energies of formation of chromium carbides, Metall. Mater. Trans. A Phys. Metall. Mater. Sci. 27 (7) (1996) 1919–1924.
[61] O. Kubasche, T.G. Chart, Calculation of metallurgical equilibrium diagrams from thermochemical data, J. Inst. Met. 93 (1965) 329.